Optics & Laser Technology 163 (2023) 109422

Contents lists available at ScienceDirect

Optics and Laser Technology

journal homepage: www.elsevier.com/locate/optlastec

Full length article

A novel CPA-based layered photonic structure for multipurpose sensing applications

You-Ran Wu [a,b], Rui-Yang Dong [a], Jie Xu [b], Hai-Feng Zhang [b,*]

[a] Bell Honor School, Nanjing University of Posts and Telecommunications, Jiangsu Province 210023, China
[b] College of Electronic and Optical Engineering and the College of Flexible Electronics (Future Technology), Nanjing University of Posts and Telecommunications, Jiangsu Province 210023, China

ARTICLE INFO

Keywords:
Coherent perfect absorption
Sensing structure
Layered photonic structure
Multipurpose physical quantities
Terahertz

ABSTRACT

Contrary to the traditional single-function sensor, a layered photonic structure (LPS) is proposed in this paper for multipurpose sensing based on the mechanism of coherent perfect absorption (CPA), which can simultaneously detect changes in the thickness of the dielectric layers, the refractive index, the incident angle, and the applied magnetic field intensity. Utilizing the Faraday effect of magnetized yttrium iron garnet, CPA is excited in the LPS. The transfer matrix method (TMM) is utilized to theoretically calculate the sensitivity, linear range, and figure of merit of the structures. To achieve high adaptability and a wide sensing range, the LPS provides two modulation detection methods based on CPA: phase modulation, which regulates and compensates for absorption via changing the optical phase, and frequency modulation, which utilizes the frequency band in comb-like absorption peaks. Due to the fragility of CPA, the multipurpose structure is of high precision, high-sensitivity. Furthermore, LPS benefits from its compact size and ease of fabrication. Therefore, we expect that our study will have some viable potential in the gauging arena.

1. Introduction

In recent years, with the rise of the field of Non-Hermitian optics, the inverse laser-based coherent perfect absorption (CPA) gives a feasible solution to designing thin and lightweight structures of ordinary dielectric materials with high absorption coefficients. Hence, CPA [1,2] has sparked a great deal of focus because of its potential for all-optical logical operations [3-5] and the dynamic tunability of absorption. Meanwhile, Parity- and time-reversal (PT) symmetric optics have piqued a lot of intrigue [6,7,8]. This paper introduces a one-dimensional PT-symmetric layered photonic structure (LPS) that realizes CPA. Moreover, CPA is only achieved when light waves are manipulated correctly, which requires a combination of optical absorption and optical interference. When magnetized yttrium iron garnet (YIG) is introduced into the LPS, it exhibits more outstanding optical properties. The loss induced in the structure is completely due to the absorption in the YIG rather than the outcoupling loss, which indicates the potential for detection. Conditions for realizing CPA have been theoretically deduced and implemented experimentally [1,2]. CPA has a wide range of applications in Absorbers [9,10,11], metamaterials [12,13,14], metasurface [15], semiconductor quantum well structure [16], stereometamaterials [17], thin-film grating [18], fano resonance plasmonic system [19], and many other materials or structures. It is indicated that CPA has great promise in applications.

One of the applications with potential is to design a sensing structure based on CPA. To realize CPA, the eigenvalue of the scattering matrix should be zero [20]. This means that CPA is implemented over narrow bands and has a hard time responding to broadband signals [21]. Hence, choosing the appropriate system configuration and parameters is necessary to achieve CPA. That is the inspiration for designing sensing structures based on CPA. A tiny change in analytes will result in variations in CPA, which could be detected. Designing a sensing structure based on the relationships between analytes and the system may be useful. In 2018, Elmahdy *et al.* designed a thermal sensor based on a central liquid crystal defect [22]. Shih *et al.* studied the surface plasmon resonance sensor in 2019 and detailed how different plasma materials affected the performance of the structures. Despite having a roughly 100 THz/RIU sensitivity, the linear measurement range reported is just 1.33–1.35 [23]. In 2020, Zaky *et al.* developed a refractive index gas sensor with a measurement linear range (LR) of 13.5 and an *S* up to 1.58 THz/RIU, which is based on an effective combination of the Tamm plasmon features and novel properties of porous silicon photonic

* Corresponding author.
E-mail addresses: hanlor@njupt.edu.cn, hanlor@163.com (H.-F. Zhang).

https://doi.org/10.1016/j.optlastec.2023.109422
Received 11 November 2022; Received in revised form 9 March 2023; Accepted 23 March 2023
0030-3992/© 2023 Elsevier Ltd. All rights reserved.

crystals [24]. In 2021, Rao *et al.* proposed a sensor composed of magnetized ferrite photonic crystals, which can measure RI and magnetic induction intensity based on evanescent coupling [25]. In 2021, A sensor based on the located defect mode resonance is presented by Wan *et al.*, which may be utilized to concurrently measure changes [26]. Their sensors perform well in a single detecting parameter and seldom do they focus on designing a multipurpose sensor. We believe that multipurpose sensing structure is promising. Furthermore, utilizing two approaches to modulating in LPS for detection demonstrates the structure's better environmental adaptability and selectivity, which is another unique aspect of the structure.

A multipurpose sensing structure is presented in this paper, which can detect four physical qualities and has two options to detect: frequency modulation, which utilizes the frequency band in comb-like absorption peaks, and phase modulation, which regulates and compensates for absorption via changing the optical phase. Utilizing the Faraday effect of magnetized YIG, the LPS generates CPA. Due to the fragility of CPA, the sensing LPS performs excellently. Furthermore, a one-dimensional LPS is easy to fabricate. In future studies, we will put a larger focus on enhancing performance metrics as the major research aim and extending the multitude of uses for sensing LPSs.

2. Theoretical model

In Fig. 1, the schematic diagram of the proposed LPS is plotted. The LPS is irradiated by two beams of EM waves propagating in opposite directions, reaching the surface of the structure with an incident angle θ. Two coherent electromagnetic (EM) waves interfere with each other throughout the structure, and CPA occurs. The structure is composed of three common dielectrics and two magnetized dielectrics represented by A, B, C, F_1, and F_2, respectively). The structure model is arranged symmetrically along the ***z***-direction according to "CBACCCF$_2$F$_1$F$_2$F$_1$F$_2$F$_2$F$_2$F$_1$F$_2$F$_1$F$_2$CCCABC". The thicknesses of three common dielectric layers, denoted by d_A, d_B, and d_C, are $d_A = 14.6$ μm, $d_B = 15.3$ μm, and $d_C = 8.5$ μm. Two magnetized dielectrics are the YIG [27] and are in different magnetic field configurations. F_1 and F_2 denote the magnetized YIGs with thicknesses $d_{F1} = 16.8$ μm, and $d_{F2} = 15.2$ μm, and their magnetic field intensity is denoted by H_{01} and H_{02}. Concerning YIG, the permittivity of the YIG is $\boldsymbol{\varepsilon_{F1}} = \boldsymbol{\varepsilon_{F2}} = \boldsymbol{\varepsilon_{YIG}} = 15$ [28]. To realize CPA, the refractive index values are fixed to $n_A = 2.25$, $n_B = 3.54$, and $n_C = 1.31$. Considering the specific materials, layer A can be made of titanium dioxide (TiO_2) [29], layer B is composed of fused silica [30] and the material of layer C could be chosen as silica dioxide (SiO_2) [2931]. Under the TE mode, the forward and backward incident EM waves are denoted by I^+, *and* I^-, respectively, and the output EM waves, which are composed of reflected light and transmitted light, are denoted by O^+, O^-.

Due to the external magnetic field along the ***y***-direction, magnetized ferrite is an anisotropic medium [32]. Therefore, the effective permittivity of YIG is a tensor [19,33] and has the following form:

$$\widehat{\mu_f} = \begin{pmatrix} \mu_r & 0 & j\mu_k \\ 0 & \mu_0 & 0 \\ -j\mu_k & 0 & \mu_r \end{pmatrix} \tag{1}$$

where

$$\mu_r = 1 + \frac{\omega_m(\omega_0 - j\alpha\omega)}{(\omega_0 - j\alpha\omega)^2 - \omega^2} \tag{2}$$

$$\mu_k = \frac{\omega_m\omega}{(\omega_0 - j\alpha\omega)^2 - \omega^2} \tag{3}$$

Here, $\alpha = 0.02$ is the damping coefficient, $\omega_0 = 2\pi\gamma H_0$ is the resonance frequency, and $\omega_m = 2\pi\gamma M_s$ is the circular frequency of YIG [32], where $\gamma = 2.8$ GHz·Oe^{-1} is the gyromagnetic ratio, H_0 is the magnetic field strength, and $M_s = 1780$ Oe is the saturation magnetization. In the proposed structure of this article, $H_{f1} = 0.85$ T, $H_{f2} = 0.575$ T.

The effective RI is [28]:

$$n_{YIG} = \sqrt{\frac{(\mu_r^2 + (j\mu_k)^2)\cdot\varepsilon_{YIG}}{\mu_r}} \tag{4}$$

Under TE polarization, the electric and magnetic field can be presented as $\boldsymbol{E} = (0, E_y, 0)e^{-j\omega t}$, $\boldsymbol{H} = (H_x, 0, H_z)e^{-j\omega t}$, respectively. Based on Maxwell's equation, an equation for $\boldsymbol{E_y}$ is attained:

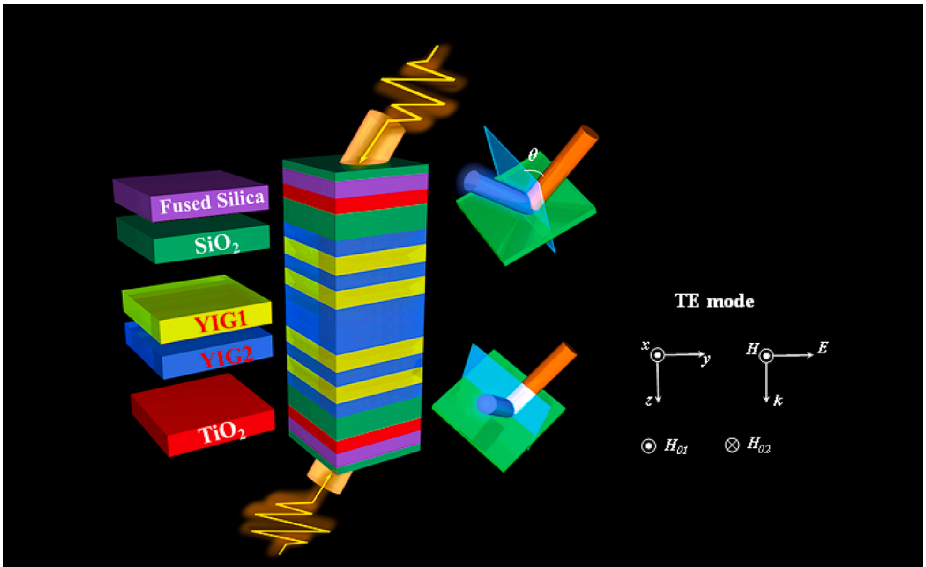

d_A	d_B	d_C	d_{F1}	d_{F2}	n_A	n_B	n_C	ε_{YIG}
14.6 μm	15.3 μm	8.5 μm	16.8 μm	15.2 μm	2.25	3.54	1.31	15

Fig. 1. Schematic diagram of the proposed structure.

$$\frac{\partial^2 E_y}{\partial x^2}+\frac{\partial^2 E_y}{\partial z^2}+k_{TE}^2 E_y=0 \tag{5}$$

$$k_{TE}=\frac{\omega}{c}\sqrt{\frac{\left(\mu_r^2+(j\mu_k)^2\right)\cdot\varepsilon_{YIG}}{\mu_r}}$$

Based on the boundary conditions, the transmission matrix can be deduced [34]:

$$M_{TE}=\begin{pmatrix}\cos(k_{TE_z}d_i)+\sin(k_{TE_z}d_i)\cdot\frac{k_{TE_x}\mu_k}{k_{TE_z}\mu_r} & -\frac{j}{\eta_{TE}}\left[1+\left(\frac{k_{TE_x}\mu_k}{k_{TE_z}\mu_r}\right)^2\right]\cdot\sin(k_{TE_z}d_i)\\ -j\eta_{TE}\sin(k_{TE_z}d_i) & \cos(k_{TE_z}d_i)-\sin(k_{TE_z}d_i)\cdot\frac{k_{TE_x}\mu_k}{k_{TE_z}\mu_r}\end{pmatrix} \tag{6}$$

where$\eta_{TE}=\frac{1}{\cos\theta}\sqrt{\frac{\mu_0}{\varepsilon_0}}\cdot\sqrt{\frac{\left(\mu_r^2+(j\mu_k)^2\right)}{\mu_r\cdot\varepsilon_{YIG}}}$,$k_{TE_y}=k_{TE}\sin\theta_f$,$k_{TE_x}=k_{TE}\cos\theta_f$, and θ_f is the incident angle towards the ferrite of light.

As for conventional dielectric layers, the transfer matrix is [35]:

$$M_j=\begin{pmatrix}\cos\delta_i & -j\sin\delta_i/\eta_i\\ -j\eta_i\sin\delta_i & \cos\delta_i\end{pmatrix}(i=A,B,C) \tag{7}$$

where $\delta_j=\eta_j d_j\cos\theta_j\cdot\frac{2\pi}{\lambda}$ and$\eta_{lj}=\sqrt{\frac{\varepsilon_0}{\mu_0}}\eta_j\cos\theta_j$.

When the EM wave passes through the proposed structure, the entire transmission matrix, which connected the input and output EM field can be deduced by analogy [35]:

$$\begin{pmatrix}E_1\\H_1\end{pmatrix}=\left(M_C M_B M_A M_C^3\left(M_{f2}M_{f1}\right)^2 M_{f2}^3\left(M_{f1}M_{f2}\right)^2 M_C^3 M_A M_B M_C\right)\cdot\begin{pmatrix}E_{N+1}\\H_{N+1}\end{pmatrix}$$

$$=\begin{pmatrix}m_{11} & m_{12}\\ m_{21} & m_{22}\end{pmatrix}\cdot\begin{pmatrix}E_{N+1}\\H_{N+1}\end{pmatrix} \tag{8}$$

The reflection coefficient R_c and transmission coefficient T_c are as follows [36],

$$R_c=|r|^2 \tag{9}$$

$$T_c=|t|^2 \tag{10}$$

$$r=\frac{(m_{11}+m_{12}\eta_{N+1})\eta_0-(m_{21}+m_{22}\eta_{N+1})}{m_{11}\eta_0+m_{12}\eta_0\eta_{N+1}+m_{21}+m_{22}\eta_{N+1}} \tag{11}$$

$$t=\frac{2\eta_0}{m_{11}\eta_0+m_{12}\eta_0\eta_{N+1}+m_{21}+m_{22}\eta_{N+1}} \tag{12}$$

And $\eta_0=\eta_{N+1}=\sqrt{\frac{\varepsilon_0}{\mu_0}}\cdot\cos\theta_0$ in the TE mode.

Hence, the absorption can be presented as:

$$A=1-|r|^2-|t|^2 \tag{13}$$

Considering the interaction of two counter-propagating EM waves, the forward and backward scattering EM fields (O_+ and O_-) can be obtained from the incident of forward and backward waves (I_+ and I_-), respectively, through the following matric relationship:

$$\begin{pmatrix}O_+\\O_-\end{pmatrix}=S\begin{pmatrix}I_+\\I_-\end{pmatrix}=\begin{pmatrix}t_+ & r_-\\ r_+ & t_+\end{pmatrix}\begin{pmatrix}I_+\\I_-\end{pmatrix} \tag{14}$$

Due to the symmetry of the LPS, the transmission and reflection coefficients in the front and rear are equal in numerical, simplifying with $t_+=t_-=t$, $r_+=r_-=r$. As a result, the scattering waves can be expressed as [37]

$$O_+=t|I_+|e^{i\phi_+}+r|I_-|e^{i\phi_-} \tag{15}$$

$$O_-=r|I_+|e^{i\phi_+}+t|I_-|e^{i\phi_-} \tag{16}$$

where φ_+, and φ_- are the phases of two incident waves.

For a two-port structure, the joint absorption may be written as:

$$A_c=1-\frac{|O_+|^2+|O_-|^2}{|I_+|^2+|I_-|^2} \tag{17}$$

With these equations, the absorption of the two-port system can be indicated as:

$$A_c=1-(|t|-|r|)^2-2|t||r|\left(1+\frac{2|I_+||I_-|\cos\Delta\varphi_1\cos\Delta\varphi_2}{|I_+|^2+|I_-|^2}\right) \tag{18}$$

where $\Delta\varphi_1=$ Arg(t)-Arg(r), where Arg() represents the argument principal value of the plural and $\Delta\varphi_2=\varphi_+-\varphi_-$.

To reach perfect absorption, the condition (1) $|I_+|=|I_-|$, (2) $|t|=|r|$, (3) $\cos\Delta\varphi_1\cos\Delta\varphi_2=-1$ should be satisfied. Besides, what can be inferred is that the absorption can be modulated from 1 to 0 by changing the optical phase when the three conditions above are met.

3. Results and discussions

Utilizing the special properties of LPS, one could choose two ways to detect physical quantities. Sensing structures designed under this principle have great advantages in their measuring range and measurement accuracy. On the one hand, detecting by frequency modulation is the most extensively used because of its intuition and convenience. The injection relationship between the frequency and the variable difficult to measure directly is established. If the numerical value of the physical quantity changes, the resonance frequency will shift accordingly. Hence, one can measure these values indirectly by observing the position of the absorption peak. On the other hand, the other workable technique for sensing is to use phase modulation. Under specific structures, even a tiny change in the value of physical quantities tend to result in a considerable drop in absorption. Meanwhile, it is discovered that a unit phase shift generates the maximum fluctuation in absorptance around the absorptance of 0.5. Hence, exploiting the optical phase to maintain the absorptance at 0.5 is considered. By measuring the phase of EM waves, it is possible to calculate the value of physical quantities. The value of the optical phase difference must then be repeatedly calculated at different wavelengths to get the numerical connection between the optical phase difference and the physical quantities.

S, quality (*Q*), the figure of merit (*FOM*), and detection limit (*DL*) are crucial metrics to consider when evaluating a sensing structure, and a good LPS has greater *S*, higher *Q*, higher *FOM*, and lower *DL*. The definitions are given as follows, where Δf, $\Delta\varphi$, and Δn denote frequency, optical phase, and physical quantities change, respectively, f_T denotes the resonance frequency and *FWHM* denotes the half-height width of the absorption peak [21,38].

$$Q=\frac{f_T}{FWHM} \tag{19}$$

$$DL=\frac{f_T}{20\cdot S\cdot Q} \tag{20}$$

If frequency modulation is applied, the parameters are as follows.

$$S=\frac{\Delta f}{\Delta n} \tag{21}$$

$$FOM=\frac{S}{FWHM} \tag{22}$$

If phase modulation is applied, the parameters are as follows: *I* denote the intensity [38,39].

$$S = \frac{\Delta\varphi_2}{\Delta n} \tag{23}$$

$$FOM^* = \left(\frac{(dI/I)}{dn}\right)_{\max} \tag{24}$$

Employing the TMM, the results are determined by the deduced coherent absorption condition. A comb-like absorption peak appears in the frequency domain. As shown in Fig. 2(a) and (b), the CPA condition is satisfied only when $\cos\Delta\varphi_1$ is equal to 1 or −1. The A_c shown in **Equation (17)** is maximized when the amplitudes of the transmission coefficient are equal to the reflection coefficient with a value of 0.25 and $\cos\Delta\varphi_1\cos\Delta\varphi_0 = -1$. Fig. 2(c) indicates that the maximal absorption is 0.5 when an EM wave incident from one side. By comparing Fig. 2(c) and Fig. 2(d), it is obvious that when the absorption peak ascends from 0.5 to 1 when the CPA theory is applied to the proposed LPS. Furthermore, one can discover that the amplitude of A_c is modulated from 0 to 1 by changing the phase difference of the incident wave from 0 to π. According to Fig. 2(d), in the specific frequency domain, all of the absorption peaks are above 0.9. Taking the peak shown in Fig. 2(d) as an example, When $\varphi_0 = 30°$, the absorption peak drops from 0.9995 in $\varphi_0 = 0°$ to 0.9328. and there is a dramatic fall in $\varphi_0 = 60°$, decreasing to 0.7504, the absorption peak is around 0.5, with a value of 0.5012. Subsequently, it remains decline when $\varphi_0 = 120°$ and $\varphi_0 = 150°$, and the coherent absorption no longer exists when $\varphi_0 = 180°$. The example absorption peak has $Q = 256.4375$ when $f = 4.103$.

Based on the comb-like absorption peaks, one can study the peak therein to realize measuring, and the results are displayed in Fig. 3(a) and (b). At the frequency of 4.581 THz, both reflectance and transmittance are 0.25. Meanwhile, at the same frequency, the absorption reaches a maximum value of 0.9995, which can be considered CPA. As demonstrated in the 3-dimensional (3-D) plot in Fig. 3(c), changing the optical phase allows for arbitrary modulation of the absorbance. It is worth noting that when the optical phase difference between two beams is 180°, there is a narrow band of strong absorptance in the spectrum of absorption. The absorptance declines as the phases slowly diverge. The absorptance drops to zero when the optical phase difference is ± 180°.

To observe the effect of this energy transfer more clearly and visually, Fig. 4 illustrates the electric field distribution at the frequency point of 4.581 THz, where the amplitude of A_c reaches the peak and the coherent absorption is realized. The electric field energy varies from 500 V/m to 5000 V/m. Immense changes in energy state indicate the remarkable interaction between two beams of counter-propagating light, which contributes to improving electromagnetic absorption properties.

3.1. Detecting by frequency modulation

First of all, when LPS is applied to measure the thickness of the dielectric layer. Due to space constraints, F_1 is picked for a thorough analysis even if F_2 also has great S and LR. In the 3-D plot in Fig. 5(c) the bulk of the A_c peak amplitude is greater than 0.9, and with the thickness of the amplitude shift, the movement does not fade. Intuitively, it maintains very good linearity and high absorption in a wide range. Fig. 5 (a) shows the linear fitting equation between d_{F2} and frequency. The linear range is 14 μm–20.2 μm. In this range, the linear fitting equation of frequency is 3.876 THz–4.779 THz. The wide linear range makes its wide measuring range. The fitting curve between them is $f = -0.14472 \cdot d_{F2} + 6.78106$. In addition, in this case, we use R-square to describe its linearity. R-square is equal to 0.99862, demonstrating that its linearity remains excellent, which is propitious to design a sensing structure. Fig. 5(b) points out the variation of *FOM* and *Q* values under the corresponding thickness. The average *FOM* and *Q* values are 7.177 μm^{-1} and 212.67, respectively. The data indicate that both *FOM* and *Q* increased substantially before they reach a peak of 8.31724 $\mu m^{-1}$and

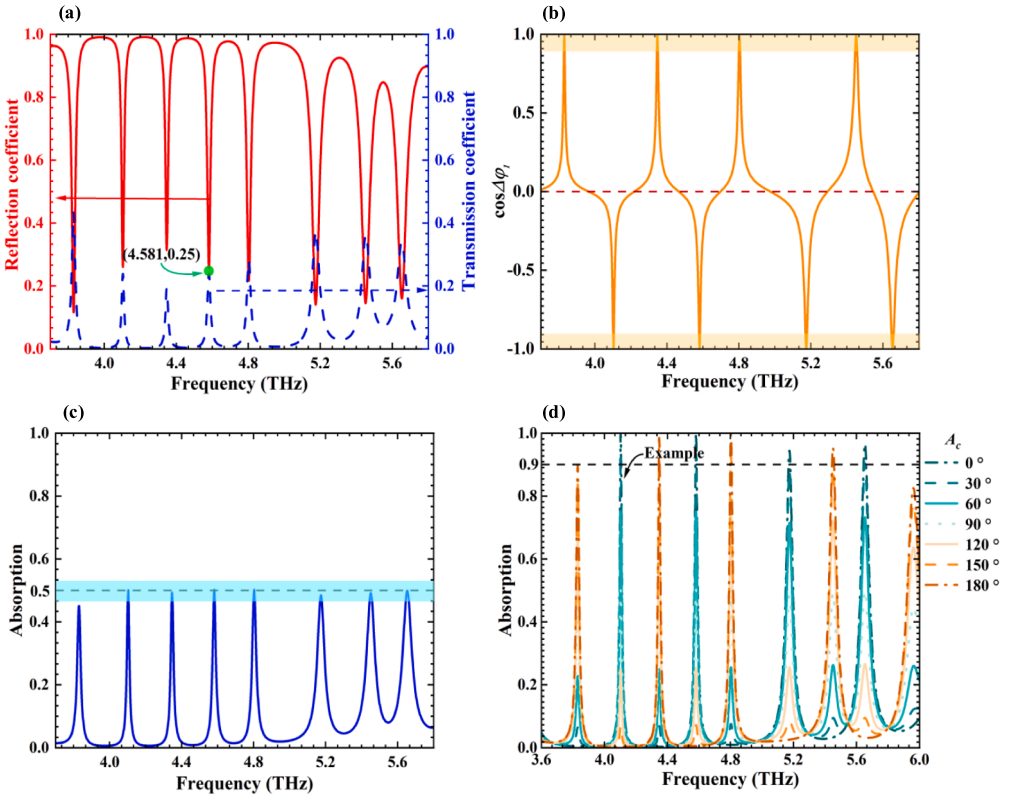

Fig. 2. When $\theta = 0°$, relative criteria to realize CPA and the phase modulation properties. (a) The relation between the frequency and the transmission of a forward EM wave and the reflection of a backward EM wave. (b) The CPA condition is satisfied only when $\cos\Delta\varphi_1$ is equal to 1 or −1. (c)The absorption curve of a one-sided incident wave. (d) change the amplitude of CPA when φ_0 varies from 0 to π.

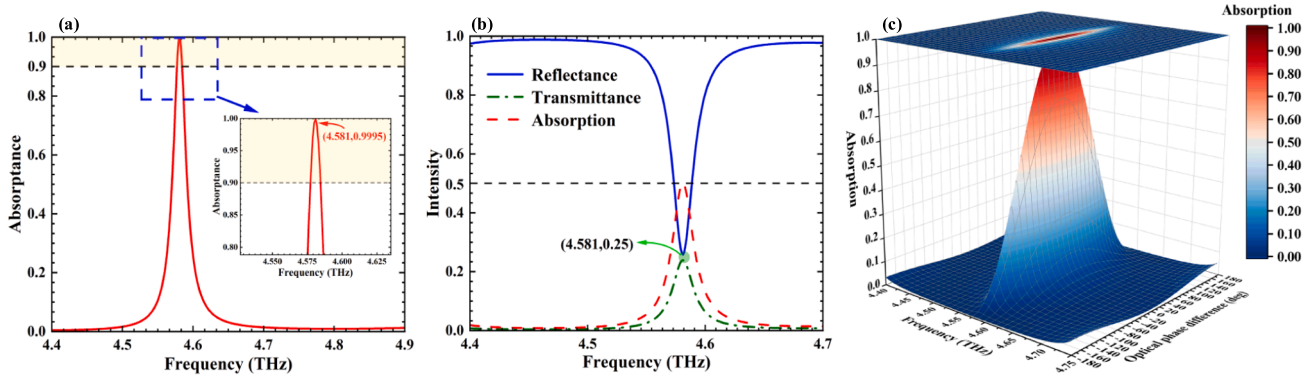

Fig. 3. (a)The absorption of LPS curve when CPA is implemented. The absorption peak, which has an intensity of 0.9995, may be located at 4.581 THz. (b) The reflection and transmission curve in the situation of one-side incidence. (c) The 3-D plot demonstrates the link between the optical phase difference and the absorption.

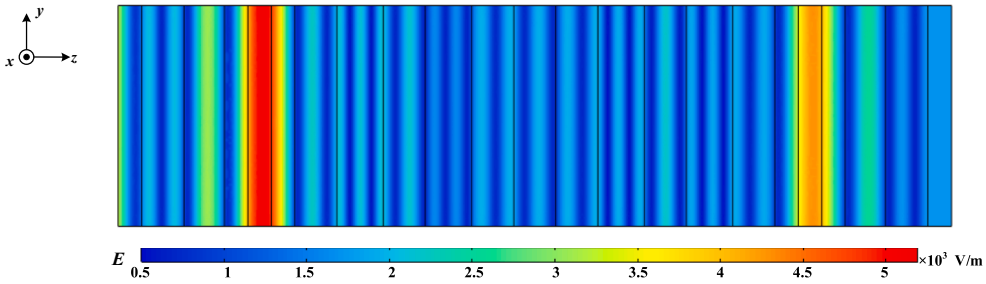

Fig. 4. The distribution of the electric field at the frequency of 4.581 THz.

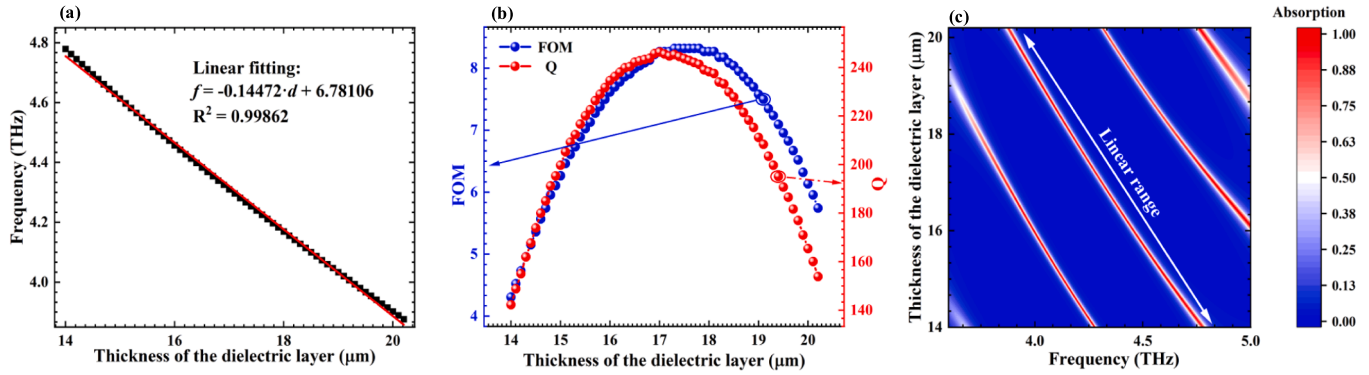

Fig. 5. (a) The linear relationship between the frequency corresponding to d_{F2} that increases at equal intervals. (b) *FOM* and *Q* values at different d_{F2}. (c) The 3-D plan view of the comb-like *Ac* peaks with d_{F2} changes.

246.30, respectively, and there are slumps until 20.2 μm. By calculation, it has an average *DL* of 0.0071. The board LR together with the high value of *FOM* and *Q* indicates the proposed LPS is characterized by a wide range and high accuracy.

Secondly, the structure also performs exceptionally well when is applied to detect the magnetic field intensity. Fig. 6(c) depicts the location of the A_c peaks as the magnetic field intensity changes. Most absorption peaks in the LR area of detection had an amplitude of more than 0.9, with the greatest being 1.0000. With coherent frequency points and excellent linearity, the magnetic field intensity varies from 0.525 T to 0.605 T, and the *Ac* amplitude is more than 0.9. The precise data analysis is displayed in Fig. 6(a) and (b). The linear frequency-magnetic field intensity fitting equation is $f = -2.57451 \cdot H_2 + 6.65989$ for the range of 5.114 THz to 5.414 THz, and the *S* may be obtained by a value of 2.57451 THz/T. Additionally, the R-square, equal to 0.98774, illustrates the linearity of this equation and shows that it satisfies the specifications of the sensing structure intended for it. When $H_2 = 0.605$ T and $f = 5.114$ THz are used, the *Q* and *FOM* are determined to be 108.81 and 54.78 T^{-1}, respectively. As demonstrated in Fig. 6(b), the values of *FOM* and *Q* somewhat rise as the frequency decreases. Additionally, its values are 46.81 T^{-1} and 96.782 when $f = 5.323$ THz. Furthermore, the average *DL* value is 0.0009, which explains the LPS makes it easier to distinguish absorption peaks, making measurements more convenient. The ferrite layer must be selected as the sensitive area since A_c peaks are more susceptible to the applied magnetic field when measuring the magnetic field intensity. The high values of *Q* and *FOM* and low values of *DL* indicate small measurement errors and excellent sensing resolution.

Thirdly, the LPS may be used to gauge the RI of analytes C. The measurement principle is the optical phase velocity changes when the RI

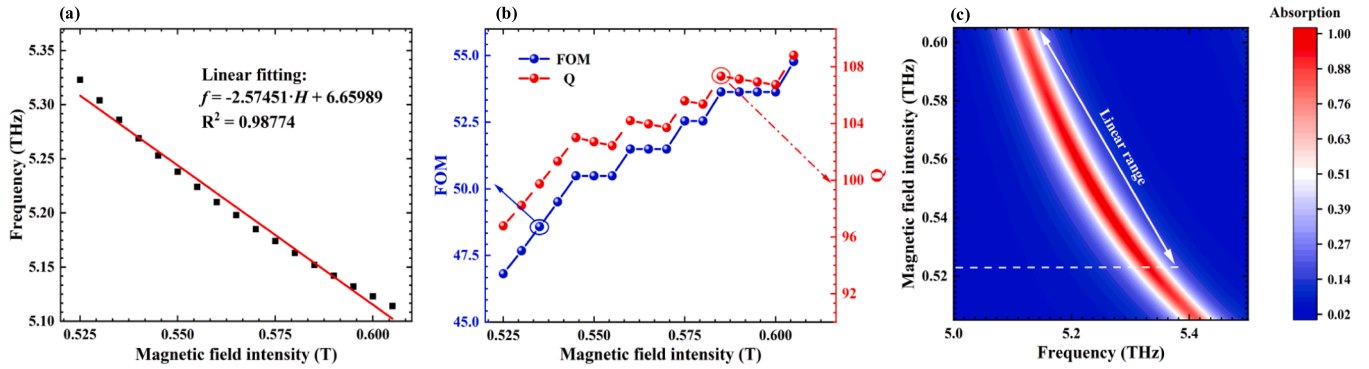

Fig. 6. (a) The linear relationship between the frequency corresponding to H_2 that increases at equal intervals. (b) *FOM* and *Q* values at different H_2. (c) The 3-D plan view of the comb-like A_c peaks with H_2 changes.

of the dielectric layer changes. As it moves through, it alters, leading to a mismatch between the transmission properties of the system and the prerequisites for CPA. This disparity results in a substantial fluctuation in absorptance, which may be utilized to identify the RI. Fig. 7(c) depicts the pattern of the position of A_c peaks shift as the refractive index varies. In the range covered by the frequency, the change is from 4.541 THz to 4.565 THz. Most of the comb-like absorption peaks depicted in the figure have an absorption amplitude larger than 0.9, and the amplitude does not diminish when the position of the absorption peak changes. Fig. 7(a) and (b) display the linear fit curves for refractive index and frequency. The range of the refractive index's linear change is 1–1.29. The extremely linear and appropriate for sensing LPS design linear fit curve at R-square = 0.98832 is $f = 0.08889 \cdot n_c + 4.45331$. With a computed *S* of 0.08889 THz/RIU, the average *Q* and *FOM* are 243.8177 and 4.819 RIU^{-1}. As the frequency increase, their values fluctuate in steps, reaching the peak of 253.2 and 5.000 RIU^{-1}, respectively. Besides, the average *DL* of 0.010 can be obtained through the calculation of **Equation (20)**. The excellent *S* and *Q* values express the sensing structure is sensitive to the tiny changes in RI, which shows the good properties of the LPS for sensing applications.

The performance characteristics when utilized as an angle sensing LPS are described in this work because there are few sensors for measuring the incidence angle. Through various angles of incidence, the LPS modulates absorption for detection. Fig. 8(c) displays a 3-D planer plot showing the position of the absorption peaks with the incident angle changes. When the absorption is assured to be large, the frequency changes from 4.59 THz to 4.70 THz, and the incident angle satisfied an excellent positive linear relationship with frequency. Within the LR, all absorption peaks exceed 0.9. The fitting curve is shown in Fig. 8(a). Their linear fitting equation, $f = 0.143239 \cdot \theta + 4.55$, has a perfect R-square value of 1 and guarantees a solid linear connection. In addition, the *S* of this angle sensing structure is determined to be 0.14332 THz/rad for the LR 16°~60° of the incident angle change. As can be observed in Fig. 8(b), The overall value of *Q* and *FOM* goes up first and then down, reaching the maximum value of 220.915 and 6.821 rad^{-1}. Their average values are 217.71 and 6.713 rad^{-1}, respectively, and it also has an average *DL* of 0.0074. The great values of *Q* and suitable *DL* demonstrate the high precision of the structure.

3.2. Detecting by phase modulation

Phase modulation can also be applied in measuring the thicknesses of the dielectric layers. It is evident from Fig. 9(c) that even a slight change in d_c results in a large fall in absorption, and exploiting the optical phase to raise the absorption back is considered here. The property is suitable for designing a phase-modulation sensing structure. The absorptions are 0.882, 0.800, 0.706, 0.621, 0.564, and 0.545 when d_c is from 9 μm to 10.5 μm at intervals of 0.3 μm. Meanwhile, the frequency of absorption peak varies quite small. As seen in Fig. 9(a) and (b), the linear relationship between the optical phase difference and d_c is formed. For the LR of 9 μm–10.5 μm, the linear optical phase difference-d_c fitting equation is $\Delta\varphi_2 = -35.3382 \cdot d_c + 406.235$, which has a high *S* value of 35.3382°/μm. At the same time, its R-square value reaches 0.98939, which represents high linearity and small measurement error. The values of *FOM* and *Q* are 276.728 μm^{-1} and 44.153 when $d_c = 10.5$ μm and $\Delta\varphi_2 = 37°$. As the optical phase difference rises, the value of *FOM* and *Q* increase accordingly. Correspondingly, for $\Delta\varphi_2 = 85°$, its values are 449.024 μm^{-1} and 71.92. Their average values are 365.442 μm^{-1} and 58.50, respectively. In addition, the calculated *DL* is determined to be 0.0014. The high value of *FOM* and small *DL* show the excellent

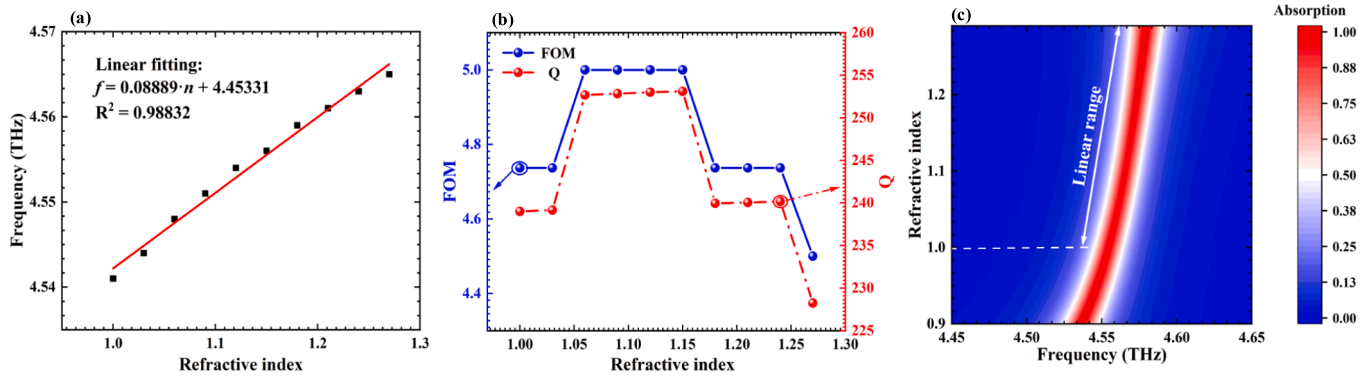

Fig. 7. (a) The linear relationship between the frequency corresponding to n_c that increases at equal intervals. (b) *FOM* and *Q* values at different n_c. (c) The 3-D plan view of the comb-like A_c peaks with n_c changes.

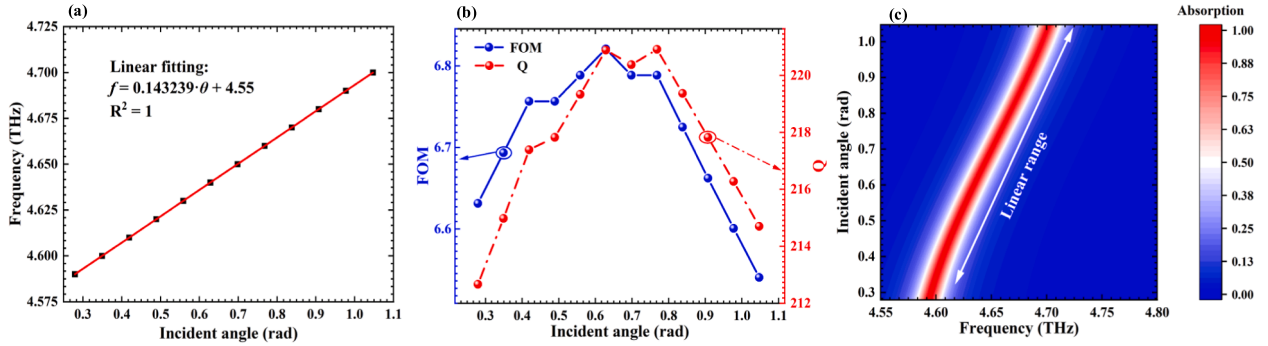

Fig. 8. (a) The linear relationship between the frequency corresponding to θ that increases at equal intervals. (b) *FOM* and *Q* values at different θ. (c) The 3-D plan view of the comb-like A_c peaks with θ changes.

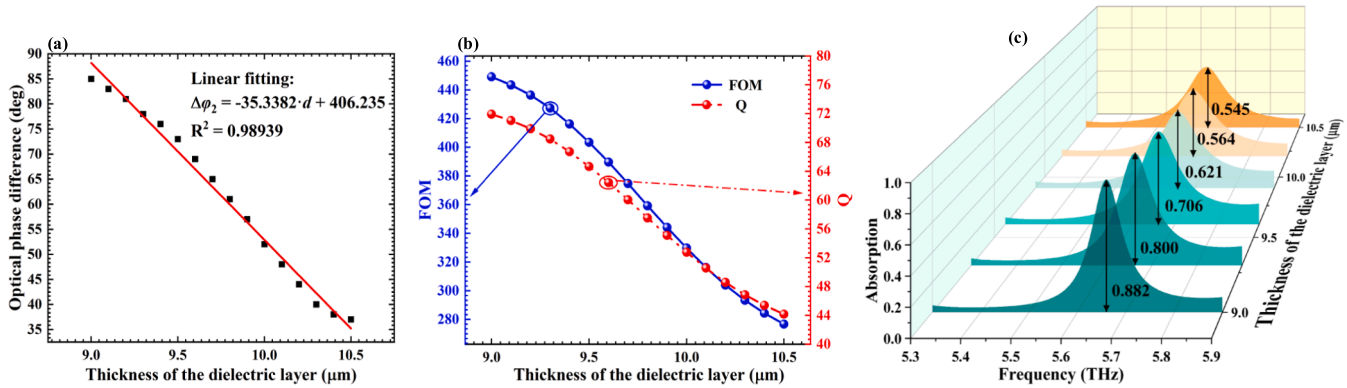

Fig. 9. (a) The linear relationship between the optical phase difference corresponding to d_c that increases at equal intervals. (b) *FOM* and *Q* values at different d_c. (c) The absorptance of the proposed structure versus frequency and optical phase difference for different d_c.

performance of the LPS. The detecting range here is not to be overlapping with the range of frequency-modulate detection, which widens the measuring range of the sensing structure.

When measuring the magnetic field intensity, the structure also exhibits superb. Considering that even a tiny change in H_{01} causes a significant drop in absorption, as seen in Fig. 10(c), the sensing LPS shows the potential of using the optical phase to increase the absorption back up to measuring H_{01}. When H_{01} is varied from 0.56 T to 0.92 T at 0.06 T intervals, the absorption peaks are 0.853, 0.735, 0.641, 0.578, 0.538, 0.513, and 0.499. As illustrated in Fig. 10(a) and (b), the linear connection between the optical phase difference and H_{01} is generated. The optical phase difference - H_{01} fitting equation for the LR of 0.56 T–0.9 T is $\Delta\varphi_2 = -216.835 \cdot H_{01} + 210.232$, with a high R-square value of 0.99592 and determined *S* of 216.835°/T. When $H_{01} = 0.56$ T and $\Delta\varphi_2 = 85°$ are used, the *FOM* and *Q* are ascertained to be 3496.774 T^{-1} and 97.258, respectively. With the optical phase difference decreasing, their value decreases at first and then increases. The outstanding *FOM* with an average value of 1881.833 T^{-1}. Moreover, the *DL* value of the LPS is 0.00002. The considerable numerals of *S*, *FOM*, and *DL* explain that the proposed structure is sensitive to the changes in H_{01} and suited for sensing.

The RI may also be measured via phase modulation. Fig. 11(c) shows a 3-D plan view of the A_c peak with RI changes. The phase velocity of light as it flows through the dielectric layer changes as its refractive

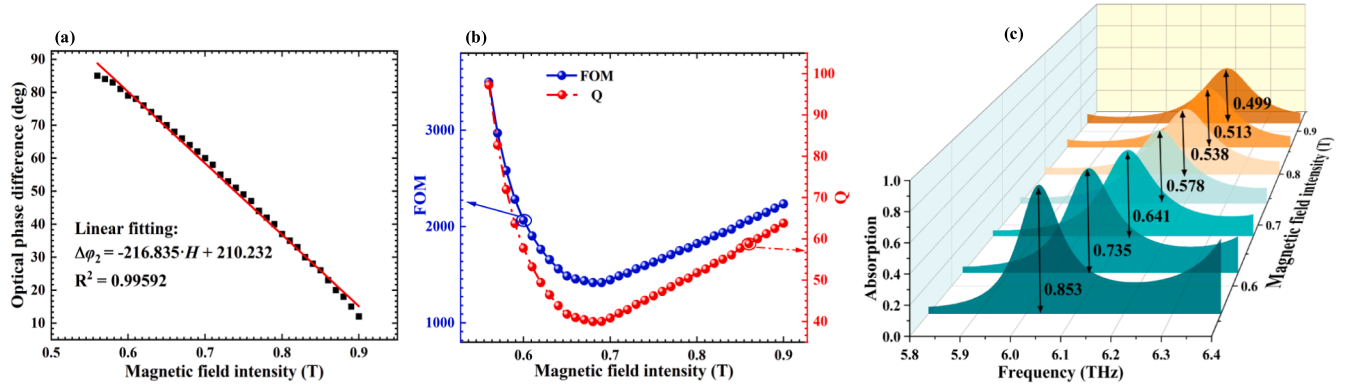

Fig. 10. (a) The linear relationship between the optical phase difference corresponding to H_{01} that increases at equal intervals. (b) *FOM* and *Q* values at different H_{01}. (c) The absorptance of the proposed structure versus frequency and optical phase difference for different H_{01}.

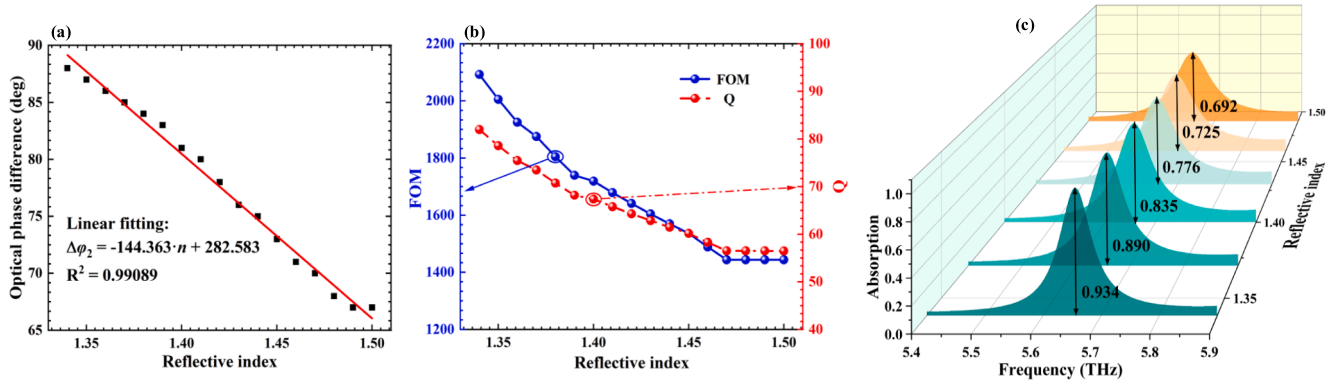

Fig. 11. (a) The linear relationship between the optical phase difference corresponding to n_c that increases at equal intervals. (b) *FOM* and *Q* values at different n_c. (c) The absorptance of the proposed structure versus frequency and optical phase difference for different n_c.

index changes, which causes a mismatch between the system's transmission characteristics and the parameters needed to achieve CPA. This disparity results in a substantial disparity in absorptance, which may be utilized to identify the RI. When n_c differs from 1.34 to 1.5 at 0.03 intervals, the absorption peaks are 0.934, 0.890, 0.835, 0.776, 0.725, and 0.692, respectively. The linear fitting curve is shown in Fig. 11(a). A negative correlation exists between the optical phase difference and the RI. Within the LR of 1.34–1.50, the fitting equation is $\Delta\varphi_2 = -144.363 \cdot n_c + 282.583$, with the calculated R-square being 0.99089. A high R-square indicates a good linear fit. One can also learn that the *S* of the structure is 144.363°/RIU. Changes in *FOM* and *Q* values at different n_c are revealed in Fig. 11(b). When $n_c = 1.34$ and $\Delta\varphi_2 = 88°$, *FOM* and *Q* acquire values of 2092.217 RIU^{-1} and 81.97, respectively. Accordingly, the average value of *FOM* and *Q* are 1673.547 RIU^{-1} and 65.55. What's more, the obtained average *DL* value is 0.000030. To maintain the favorable properties of the LPS and a wide measuring range, the detecting range here does not intersect with the one above. Simultaneously, the substantial values of *Q*, *FOM*, and diminutive *DL* suggest the high accuracy of the sensing structure.

The structure might also be employed to determine the incident angle θ. The absorption peak with incident angle variations is shown in Fig. 12(c). When the incident angle raises from 76° to 80° at 1° intervals, the absorption significantly decreases accordingly, with values of 0.935, 0.890, 0.835, 0.776, 0.725, and 0.692. Fig. 12(a) depicts the linear fitting curve. The optical phase difference and the incident angle have a negative association. With a reported R-square of 0.98496, the fitting equation is $\Delta\varphi_2 = -102.559 \cdot \theta + 217.689$, when θ is in the LR of 76–80°. Additionally, the *S* of LPS, which is 102.559°/rad, can be found. Fig. 12 (b) focuses on the change in *FOM* and *Q* values at various incident angles. FOM and Q acquire values of 5127.95 rad^{-1} and 236.2 when $\Delta\varphi_2 = 74°$ and $\theta = 1.396$ rad. As the angle of incidence grows, the values of *Q* and *FOM* fluctuate and increase. Furthermore, their average values are 4992.3 rad^{-1} and 2229.93, respectively. The *DL* can be acquired as well, with an average value of 0.000010. According to the numerical above, obviously, at a large incident angle range, the proposed structure shows good properties. Combining the two detecting methods above, the sensor can measure essentially arbitrary angles, which is a unique feature of an optical structure.

As shown in Table.1, the proposed model in this study is more essential than traditional sensors owing to its multi-physics measuring capacity and use of coherent absorption theory in sensing. By comparing with **Refs.** [40] and [41], the sensor they designed has decent sensitivity, but the range of measurement is too narrow to detect. Meanwhile, a single measurement volume sensor has limitations. When compared to **Ref.** [43], the presented LPS has a greater *FOM* when measuring the RI. The *FOM* is positively connected with the sensitivity when measuring each physical quantity because the structure is intended to have a limited impact on the relative bandwidth of the absorption peaks when measuring various parameters. In comparison to **Refs.** [42] and [44], the multipurpose structure has a broader LR, when it comes to measuring single physical quality. Generally speaking, the multipurpose sensor features a wide variety of detecting quantities, a wide detecting range, and high sensitivity, which is promising for application.

In this paper, a one-dimensional LPS is proposed, which is composed of common dielectric and YIGs. TiO2, SiO2, and fused silica can be selected as the common dielectric. and YIG exhibits special optical properties by modulating the strength of the applied magnetic field. By the calculation of the transmission matrix method, we obtain the

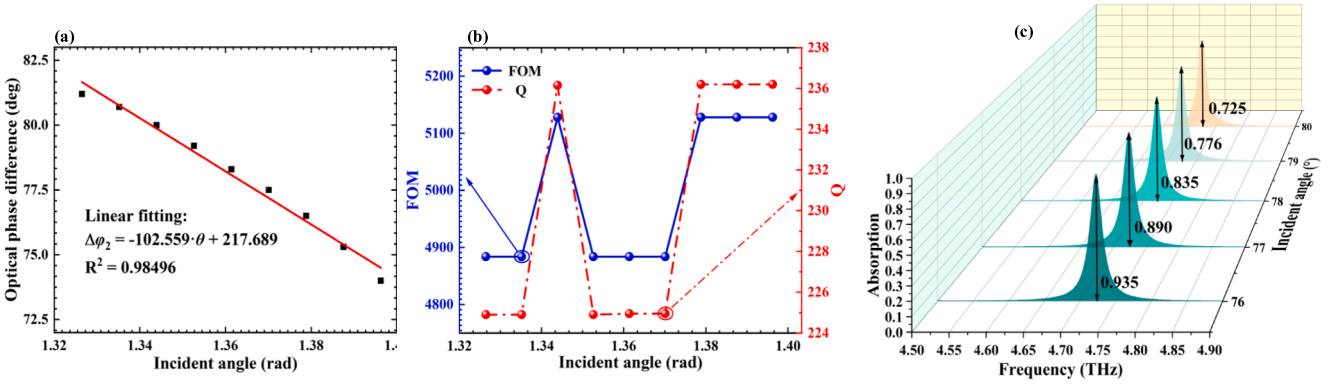

Fig. 12. (a) The linear relationship between the optical phase difference corresponding to θ that increases at equal intervals. (b) *FOM* and *Q* values at different incident angle. (c) The absorptance of the proposed structure versus frequency and optical phase difference for different θ.

Table 1
Comparison of optimal parameters between reference and this work.

Ref.	Physical quantity	LR	S	FOM/ FOM*	Physical mechanism
[40]	Thickness	None	None	None	Surface Plasmon Resonance
	Magnetic field	None	None	None	
	Refractive index	1.33–1.34	236 THz·RIU^{-1}	None	
	Incidence angle	None	None	None	
[41]	Thickness	None	None	None	Surface Plasmon Resonance
	Magnetic field	None	None	None	
	Refractive index	1.47–1.48	10.3 THz·RIU^{-1}	None	
	Incidence angle	None	None	None	
[42]	Thickness	None	None	None	Multiple Fano Resonance
	Magnetic field	None	None	None	
	Refractive index	1.3–1.4	765 nm·RIU^{-1}	1098 RIU^{-1}	
	Incidence angle	None	None	None	
[43]	Thickness	None	None	None	Frequency Selective Surfaces Absorber
	Magnetic field	None	None	None	
	Refractive index	1–3.16	1.311 GHz·RIU^{-1}	7.28 RIU^{-1}	
	Incidence angle	None	None	None	
[44]	Thickness	None	None	None	Magnetic-Fluid-Integrated Fiber Interferometer
	Magnetic field	0.004–0.016 T	346.4 nm·T^{-1}	none	
	Refractive index	None	None	None	
	Incidence angle	None	None	None	
[45]	Thickness	None	None	None	Optical Tamm State
	Magnetic field	None	None	None	
	Refractive index	2–2.7	32.3 THz·RIU^{-1}	100 RIU^{-1}	
	Incidence angle	25~70°	0.5 THz·deg^{-1}	0.5 deg^{-1}	
This work	Thickness	14–20.2 μm	0.14472 THz·μm^{-1}	8.31724 μm^{-1}	Frequency Modulation (CPA)
	Magnetic field	0.525–0.605 T	2.57451 THz· T^{-1}	54.78 T^{-1}	
	Refractive index	1–1.29	0.08889 THz·RIU^{-1}	4.73684 RIU^{-1}	
	Incidence angle	16~60°	0.143239 THz·rad^{-1}	6.821 rad^{-1}	
	Thickness	9–10.5 μm	35.3382°·μm^{-1}	449.024 μm^{-1}	Phase Modulation (CPA)
	Magnetic field	0.56–0.9 T	216.835°·T^{-1}	3496.774 T^{-1}	
	Refractive index	1.34–1.5	144.363°·RIU^{-1}	2092.217 RIU^{-1}	
	Incidence angle	76–80°	1102.559°·rad^{-1}	5127.95 rad^{-1}	

absorption rate of coherent absorption and perform the sensing function using the following two options: frequency modulation, which utilizes the frequency band in comb-like absorption peaks, and phase modulation, which regulates and compensates for absorption via changing the optical phase. We apply two methods for sensing each of the four physical quantities: thickness, refractive index, incident angle, and applied magnetic field intensity. By calculating the S, FOM, and DL values of the sensing structure, we found that the sensing structure has the advantages of high sensitivity and high measurement accuracy. In addition, the structure is based on a one-dimensional LPS, which enables it to have the advantage of being easy to fabricate and compact in size.

4. Conclusion

The research presents a unique multi-purpose detection method based on is introduced by proposing a hypothetical sensing structure model that employs frequency modulation and phase modulation for measuring. This sensing LPS can detect the thickness of the dielectric, the magnetic field intensity, the refractive index, and the incident angle and examine the performance of these four conditions. Substantial values of *S*, *FOM*, and *Q* demonstrate the excellent working performance of LPS. About phase modulation, through the analysis, it is concluded that the LR and *S* of the sensing structure when it is used for sensing d_3 are as follows: 9 μm–10.5 μm, 35.3382°/μm. If used to detect H_{01}, the corresponding parameters are 0.56 T–0.9 T, 216.835°/T. When it is applied to the measurements of n_3, the related values are 1.34–1.50, 144.363°/ RIU. If used to measure the incident angle θ, the relevant values are 76–80, 1102.559°/rad. Meanwhile, when it comes to frequency modulation, in the case of being used to measure d_{F2}, the relevant values are 14 μm–20.2 μm, 0.14472 THz/μm. On condition that H_{02} is measured, the homologous parameters are 0.505 T–0.605 T, 2.91974 THz/T. As for θ and n_3, the corresponding values are 0.81–1.2, 0.152727 THz/RIU, and 16–60, 0.143239 THz/rad. Combining the two gauging methods, the proposed structure has a broad detecting range. The innovation point of study and significant aspect is the use of CPA theory to detect many quantities from different physics with a single LPS by phase and frequency modulation. In the fields of pressure sensing, photosensitive sensing, biosensing, and absorber designing, it is hoped that this study will be widely used. This theoretical study broadens the usage of CPA in sensing applications and serves as a guide for foreseeable applications.

CRediT authorship contribution statement

You-Ran Wu: Data curation, Formal analysis, Investigation, Writing – original draft, Visualization. **Rui-Yang Dong:** Software, Validation. **Jie Xu:** Software, Validation. **Hai-Feng Zhang:** Conceptualization, Methodology, Supervision, Writing – review & editing.

Declaration of Competing Interest

The authors declare that they have no known competing financial interests or personal relationships that could have appeared to influence the work reported in this paper.

Data availability

Data will be made available on request.

References

[1] W. Wan, Y. Chong, L. Ge, H. Noh, A.D. Stone, H. Cao, Time-reversed lasing and interferometric control of absorption, Science 331 (6019) (2011) 889–892.
[2] Y. D. Chong, L. Ge, H. Cao, and A. D. Stone. "Coherent Perfect Absorbers: Time-Reversed Lasers." Physical review letters 105.5(2010):P.053901.1-053901.4.
[3] R.E. Meymand, A. Soleymani, N. Granpayeh, All-optical AND, OR, and XOR logic gates based on coherent perfect absorption in graphene-based metasurface at terahertz region, Opt. Commun. 458 (2020), 124772.
[4] M. Papaioannou, E. Plum, J. Valente, E.T. Rogers, N.I. Zheludev, All-optical multichannel logic based on coherent perfect absorption in a plasmonic metamaterial, APL Photonics 1 (9) (2016), 090801.

[5] M. Papaioannou, E. Plum, J. Valente, E.T. Rogers, N.I. Zheludev, Two-dimensional control of light with light on metasurfaces, Light Sci. Appl. 5 (4) (2016) e16070–e.
[6] S. Longhi, L. Feng, PT-symmetric microring laser-absorber, Opt. Lett. 39 (17) (2014) 5026–5029.
[7] D.G. Baranov, A. Krasnok, T. Shegai, A. Alù, Y. Chong, Coherent perfect absorbers: linear control of light with light, Nat. Rev. Mater. 2 (12) (2017) 1–14.
[8] Y.D. Chong, L. Ge, A.D. Stone, Pt-symmetry breaking and laser-absorber modes in optical scattering systems, Phys. Rev. Lett. 106 (9) (2011), 093902.
[9] B.X. Wang, G. Duan, C. Xu, J. Jiang, W. Xu, F. Pi, Design of multiple-frequency-band terahertz metamaterial absorbers with adjustable absorption peaks using toothed resonator, Mater. Des. 111586 (2023).
[10] B.X. Wang, C. Xu, H. Zhou, G. Duan, Realization of broadband terahertz metamaterial absorber using an anti-symmetric resonator consisting of two mutually perpendicular metallic strips, APL Mater. 10 (5) (2022), 050701.
[11] B.X. Wang, W. Xu, Y. Wu, Z. Yang, S. Lai, L. Lu, Realization of a multi-band terahertz metamaterial absorber using two identical split rings having opposite opening directions connected by a rectangular patch, Nanoscale Advances 4 (5) (2022) 1359–1367.
[12] B.X. Wang, Y. He, P. Lou, H. Zhu, Multi-band terahertz superabsorbers based on perforated square-patch metamaterials, Nanoscale Advances 3 (2) (2021) 455–462.
[13] B.X. Wang, C. Xu, G. Duan, J. Jiang, W. Xu, Z. Yang, Y. Wu, Miniaturized and actively tunable triple-band terahertz metamaterial absorber using an analogy I-typed resonator, Nanoscale Res. Lett. 17 (1) (2022) 35.
[14] S. Feng, K. Halterman, Coherent perfect absorption in epsilon-near-zero metamaterials, Phys. Rev. B 86 (16) (2012), 165103.
[15] W.R. Zhu, F. Xiao, M. Kang, M. Premaratne, Coherent perfect absorption in an all-dielectric metasurface, Appl. Phys. Lett. 108 (12) (2016), 121901.
[16] C.C. Byeon, M.K. Oh, H.S. Kang, D.K. Ko, J.M. Lee, J.S. Kim, C.S. Kee, Coherent absorption spectroscopy with supercontinuum for semiconductor quantum well structure, J. Opt. Soc. Korea 11 (3) (2007) 138–141.
[17] W. Lv, J. Bing, Y. Deng, D. Duan, Z. Zhu, Y. Li, J. Shi, Polarization-controlled multifrequency coherent perfect absorption in stereometamaterials, Opt. Express 26 (13) (2018) 17236–17244.
[18] J.W. Yoon, G.M. Koh, S.H. Song, R. Magnusson, Measurement and modeling of a complete optical absorption and scattering by coherent surface plasmon-polariton excitation using a silver thin-film grating.“, Phys. Rev. Lett. 109 (25) (2012), 257402.
[19] M. Kang, Y.D. Chong, H.T. Wang, W. Zhu, M. Premaratne, Critical route for coherent perfect absorption in a Fano resonance plasmonic system, Appl. Phys. Lett. 105 (13) (2014), 131103.
[20] A. Krasnok, D. Baranov, H. Li, M.A. Miri, F. Monticone, A. Alú, Anomalies in light scattering, Adv. Opt. Photon. 11 (4) (2019) 892–951.
[21] Y. Zhang, F.P. Wu, H.F. Zhang, Theoretical Model of a RI THz Sensor Realized by Coherent Perfect Absorption With Optical Phase Modulation, IEEE Sens. J. 22 (15) (2022) 14842–14850.
[22] N.A. Elmahdy, M.S. Esmail, M.M. El-Okr, Characterization of a thermal sensor based on one-dimensional photonic crystal with central liquid crystal defect, Optik 170 (2018) 444–451.
[23] K. Shih, P. Pitchappa, M. Manjappa, C.P. Ho, R. Singh, C. Lee, Microfluidic metamaterial sensor: Selective trapping and remote sensing of microparticles, J. Appl. Phys. 121 (2) (2017), 023102.
[24] Z.A. Zaky, A.M. Ahmed, A.H. Aly, Refractive index gas sensor based on the Tamm state in a one-dimensional photonic crystal: Theoretical optimisation, Sci. Rep. 10 (1) (2020) 9736.
[25] S.S. Rao, Y.M. Liu, B.F. Wan, H.F. Zhang, Theoretical Proposal of a Multitasking Sensor Realized by the Mechanism of Nonreciprocal Absorption Evanescent Wave in the Magnetized Ferrite Photonic Crystals, IEEE Sens. J. 21 (24) (2021) 27405–27413.
[26] B.F. Wan, Y. Xu, Z.W. Zhou, D. Zhang, H.F. Zhang, Theoretical Investigation of a Sensor Based on One-Dimensional Photonic Crystals to Measure Four Physical Quantities, IEEE Sens. J. 21 (3) (2020) 2846–2853.
[27] D.L. Wood, J.P. Remeika, Effect of impurities on the optical properties of yttrium iron garnet, J. Appl. Phys. 38 (3) (1967) 1038–1045.
[28] S.J. Guo, Z.J. Li, F.Y. Li, Y. Xu, H.F. Zhang, The asymmetric optical bistability based on the one-dimensional photonic crystals composed of the defect layers containing the magnetized ferrite and nonlinear Kerr dielectric under the transverse electric polarization, J. Appl. Phys. 129 (9) (2021), 093104.
[29] J. Kischka, S. Peters, B. Gruska, M. Semtsiv, M. Chashnikova, M. Klinkmüller, W. T. Masselink, Mid-infrared optical properties of thin films of aluminum oxide, titanium dioxide, silicon dioxide, aluminum nitride, and silicon nitride, Appl. Opt. 51 (28) (2012) 6789–6798.
[30] R. Kitamura, L. Pilon, M. Jonasz, Optical constants of silica glass from extreme ultraviolet to far infrared at near room temperature, Appl. Opt. 46 (33) (2007) 8118–8133.
[31] C.Z. Tan, Determination of refractive index of silica glass for infrared wavelengths by IR spectroscopy, J. Non Cryst. Solids 223 (1-2) (1998) 158–163.
[32] Y. Sharma, S. Prasad, V. Singh, Dispersion behavior of electromagnetic wave near the resonance in 1D magnetized ferrite photonic crystals, Opt. Quant. Electron. 50 (11) (2018) 1–19.
[33] H. Mehdian, Z. Mohammadzahery, A. Hasanbeigi, Optical and magneto-optical properties of plasma-magnetic metamaterials, J. Phys. D Appl. Phys. 48 (30) (2015), 305101.
[34] S. Guo, M. Mao, Z. Zhou, D. Zhang, H. Zhang, The wide-angle broadband absorption and polarization separation in the one-dimensional magnetized ferrite photonic crystals arranged by the Dodecanacci sequence under the transverse magnetization configuration, J. Phys. D Appl. Phys. 54 (1) (2020), 015004.
[35] L. Qi, Z. Yang, F. Lan, X. Gao, Z. Shi, Properties of obliquely incident electromagnetic wave in one-dimensional magnetized plasma photonic crystals, Phys. Plasmas 17 (4) (2010), 042501.
[36] R. Ning, S. Liu, H. Zhang, B. Bian, X. Kong, “A wide-angle broadband absorber in graphene-based hyperbolic metamaterials.” The European Physical Journal-Applied, Physics 68 (2014) 2.
[37] B.F. Wan, Q.Y. Wang, H.M. Peng, H.N. Ye, H.F. Zhang, A Late-Model Optical Biochemical Sensor Based on OTS for Methane Gas and Glucose Solution Concentration Detection, IEEE Sens. J. 21 (19) (2021) 21465–21472.
[38] J. Becker, A. Trügler, A. Jakab, U. Hohenester, C. Sönnichsen, The optimal aspect ratio of gold nanorods for plasmonic bio-sensing, Plasmonics 5 (2) (2010) 161–167.
[39] S.M. Nalawade, S.S. Harnol, H.V. Thakur, Temperature and strain independent modal interferometric torsion sensor using photonic crystal fiber, IEEE Sens. J. 12 (8) (2012) 2614–2615.
[40] M.A. Gandhi, S. Nivedha, P.R. Babu, S. Sivabalan, K. Senthilnathan, Designing a refractive index based biosensor using a photonic quasi-crystal fiber. 2015 Workshop on Recent Advances in Photonics (WRAP), IEEE, 2015.
[41] Y. Kong, J. Cao, W. Qian, C. Liu, S. Wang, Multiple fano resonance based optical refractive index sensor composed of micro-cavity and micro-structure, IEEE Photonics J. 10 (6) (2018) 1–10.
[42] W. Zhang, J.Y. Li, J. Xie, R. Xu, High sensitivity refractive index sensor based on frequency selective surfaces absorber, IEEE Sensors Lett. 2 (3) (2018) 1–4.
[43] W. Wu, Y. Cao, H. Zhang, B. Liu, X. Zhang, S. Duan, Y. Liu, Compact magnetic field sensor based on a magnetic-fluid-integrated fiber interferometer, IEEE Magn. Lett. 10 (2019) 1–5.
[44] B.F. Wan, Z.W. Zhou, Y. Xu, H.F. Zhang, A theoretical proposal for a refractive index and angle sensor based on one-dimensional photonic crystals, IEEE Sens. J. 21 (1) (2020) 331–338.